International Space Planes and Hypersonic Systems and Technologies Conferences
6-9 July 2015, Glasgow, Scotland
20th AIAA International Space Planes and Hypersonic Systems and Technologies Conference

A Homotopy and Parallelization Approach for Improving the Solution Time of Hypersonic Footprints

Michael A. Bolender *
U.S. Air Force Research Laboratory, Wright-Patterson AFB, OH 45433
Michael J. Grant †and Michael Sparapany ‡
School of Aeronautics and Astronautics, Purdue University, West Lafayette, IN

To solve optimal control problems for hypervelocity vehicles in a computationally efficient manner, it is common to make assumptions that simplify the problem, such as flight at maximum lift-to-drag ratio or equilibrium glide. Such assumptions are usually taken to reduce the dimensionality of the dynamical system, and may result in analytical expressions for the control that require a numerical search over a small number of parameters instead of solving the full-order optimal control problem. However, these assumptions have been shown to not always result in favorable comparisons with the numerical solution of the "full" optimal control problem. This paper addresses the problem of trajectory optimization by utilizing known integrals-of-motion and an analysis of the behavior of the co-states for a family of trajectories. It is shown that it is possible to simultaneously reduce the dimensionality of the optimal control problem without affecting the underlying physics, and yet also provide a quality initial guess for the co-states. The latter is important for the solution of optimal control problems using indirect methods.

I. Introduction

Successful real-time implementation of air vehicle trajectory planning/guidance algorithms have utilized approximate methods that either assume some knowledge of the control and/or make assumptions to reduce the dimensionality of the dynamical system. For example, in atmospheric entry vehicles such as the Space Shuttle Orbiter, the angle-of-attack profile is often determined *a priori*, either to satisfy heating constraints or to maximize lift-to-drag ratio.[1] This implementation eliminates having guidance generate the angle-of-attack command, leaving bank angle as the only control. For example, the guidance law for the Space Shuttle Orbiter utilized bank angle to modulate energy during re-entry and used angle-of-attack corrections to a nominal profile to control heating rates.[2]

However, the desire to solve optimal control problems in real-time for use in a guidance system has been well stated in the literature.[3] Significant progress has been made in the last 20-plus years with direct optimization methods and improved computing power that recently culminated in a flight demonstration of an optimal attitude change maneuver on a satellite.[4] However, for general aircraft problems that have significantly more complex dynamics, real-time optimal control is a goal that has not been reached because convergence to a solution is still not guaranteed in a fixed number of steps.

There is a rich history of aerospace vehicle trajectory optimization literature that dates back nearly 60 years. A general theorem for optimizing cost functions of the Mayer type for aircraft and rocket trajectory

*Senior Aerospace Engineer. Associate Fellow AIAA.
†Assistant Professor. Senior Member AIAA
‡Graduate Research Assistant. Student Member AIAA

optimization that was given by Breakwell[5] that relaxed many prior assumptions. Breakwell addressed problems such as boosting a missile for maximum range by breaking the problem up into distinct phases: an ascent phase where the thrust magnitude is assumed known, but the thrust can be vectored and the angle-of-attack can be varied; an exo-atmospheric phase that is described by classical orbital mechanics; and an un-powered re-entry phase. The first-order necessary conditions were derived for each phase, and as one would expect, the solution required matching the end points for each of the different phases to obtain the complete trajectory.

Vinh addresses the solution of the footprint problem in Reference [6]. The solution that is developed assumes the vehicle flies an equilibrium glide and that the lateral range (latitude) is small. An approximate bank-angle law is then computed analytically as a function of the known terminal boundary conditions on the states. This control law was determined, in part, from integrals-of-motion for the system. However, Fahroo, et.al.[7] compared the performance of Vinh's analytical bank angle guidance law to that of a pseudospectral method, and showed that the reduction in the state space/dynamics assumed by Vinh resulted in a smaller footprint when compared to the full point-mass dynamics used in their application of a pseudospectral method.

In Reference [1], Lu and Xue discuss the difficulty of numerically solving the maximum crossrange problem for a given downrange to a desired terminal energy state. They make an assumption that the entire flight will occur at a quasi-equilibrium glide condition and are able to reduce the dimension of the state-space by eliminating the flight-path angle dynamics. A near-optimal bank angle control law is then derived in closed-form as a non-linear function of the vehicle's state. The quasi-equilibrium glide assumption also acts to remove phugoid-like oscillations in the trajectory, which arise when the problem includes all the point-mass dynamic states. Finally, the footprint problem is re-cast in terms of minimizing the distance to some desired latitude-longitude pair that is known to be unreachable. This then reduces the problem, for a single trajectory, to be solved by searching for the value of a single parameter.

Lu, Forbes, and Baldwin[8] address the gliding guidance of high lift-to-drag ratio hypersonic vehicles that are considered sub-orbital because they do not have the initial energy of re-entry vehicles, although they point out that this particular assumption is not a limiting assumption. The approach utilized an adaptive predictor-corrector algorithm for a fixed angle-of-attack profile to rapidly compute a feasible trajectory from known initial conditions to a defined terminal condition. The algorithm solved for the bank angle commands to meet defined terminal boundary conditions. The paper also provides a feedback control that utilizes a sink-rate command to eliminate phugoid motions from the optimal trajectory.

Bollino[9] has investigated the possibility of using pseudo-spectral methods in real-time for the re-entry problem that terminates at a specified window of terminal conditions. The study looked at re-computing the optimal trajectory in order to account for wind variations and other trajectory constraints. While not solved in real-time due to its implementation on a desktop computer, the study did demonstrate the robustness of the approach. Subsequently, benchmark execution times were recorded that showed the promise of this particular pseudo-spectral optimal control code for real-time control in an aerospace vehicle application.

Because of their prior use in analytical dynamics to analytically solve systems whose equations-of-motion are derived using variational methods, integrals-of-motion for aircraft and spacecraft trajectory optimization problems have been derived and utilized in various ways. Both Moyer[10,11] and Vinh[12] derive integrals-of-motion for aircraft and spacecraft for optimal control problems of the Mayer type. Moyer[11] applied Noether's Theorem to obtain integrals-of- motion that contained the co-states associated with heading, latitude, and longitude for flight over a spherical planet. Vinh,[12] on the other hand, used geometric arguments to find integrals of motion under some restrictive assumptions, such as flight at a maximum lift-to-drag ratio and over a flat Earth. However, while Moyer only computed the integrals-of-motion, Vinh[6,13] took advantage of different assumptions to use the integrals to derive a bank angle control law for flight at maximum lift-to-drag ratio. In Reference [1], the integrals-of-motion are also used to develop a bank angle control law for the footprint problem, similar to what has been done previously by Vinh.[6]

The contribution of this paper is that a homotopy and potential parallelization method for generating a

minimum terminal energy footprint for a hypervelocity aircraft is proposed that is based on the evolution of the initial co-states and integrals-of-motion using the longitude co-state (which is an integral-of-motion) as a sweeping parameter. Using the integrals-of-motion admits closed-form solutions for the heading co-state and latitude co-states, thus avoiding numerical integration of these two co-states. However, to utilize these expressions, the values of the integrals-of-motion must be known *a priori*. Information about how the initial conditions of the co-states evolve as the longitude co-state is varied can then be used to provide accurate initial guesses for the co-states, thus improving convergence of indirect methods.

II. Trajectory Optimization Problems: Mayer Formulation

A set of optimal control problems for un-powered or gliding hypersonic vehicles are considered where the performance index to be minimized is of the Mayer type

$$J = \boldsymbol{\Phi}(\boldsymbol{x}(t_f), t_f)$$

where the initial state $\boldsymbol{x}(0) = \boldsymbol{x}_0$ is given and $\boldsymbol{x}(t) \in \mathbb{R}^n$, the final time t_f is free, and $q \leq n$ terminal boundary conditions $\boldsymbol{x}(t_f)$ are specified. The dynamics of the system are given by the differential equation

$$\dot{\boldsymbol{x}} = \boldsymbol{f}(\boldsymbol{x}(t), \boldsymbol{u}(t), t)$$

where $\boldsymbol{u}(t) \in \mathbb{R}^m$ are the controls. Additionally, it is assumed that there are no constraints on either the states or the controls, nor are there path constraints.

Because the optimal control problem being considered is of the Mayer type, the Hamiltonian is then

$$\mathscr{H} = \boldsymbol{\lambda}^T \dot{\boldsymbol{x}}$$

The first-order necessary conditions for the optimal control problem (the Euler-Lagrange Equations) are:[14]

$$\dot{\boldsymbol{x}} = \frac{\partial \mathscr{H}}{\partial \boldsymbol{\lambda}} = \boldsymbol{f}(\boldsymbol{x}(t), \boldsymbol{u}(t), t) \tag{1}$$

$$\dot{\boldsymbol{\lambda}} = -\frac{\partial \mathscr{H}}{\partial \boldsymbol{x}} \tag{2}$$

$$\boldsymbol{0} = \frac{\partial \mathscr{H}}{\partial \boldsymbol{u}} \tag{3}$$

The terminal boundary conditions are then (Reference [14])

$$0 = \left.\frac{\partial G}{\partial t}\right|_{t_f} + \mathscr{H}(t_f) \tag{4}$$

$$x_i(t_f) = x_{i,f},\ i = 1, \ldots, q \tag{5}$$

$$x_i(t_f) = \text{free},\ i = q+1, \ldots, n \tag{6}$$

$$\lambda_i(t_f) = \left.\frac{\partial G}{\partial x_i}\right|_{t_f} + \nu_i,\ i = 1, \ldots, q \tag{7}$$

$$\lambda_i(t_f) = 0,\ i = q+1, \ldots, n \tag{8}$$

where the end-point function for the purposes of this paper is defined as

$$G \triangleq \boldsymbol{\Phi}(\boldsymbol{x}(t_f), t_f) + \sum_{i=1}^{q} \nu_i (x_i(t_f) - x_{i,f}) \tag{9}$$

Remark 1 *Equation 9 is a special case of the most general case, where one can define a manifold* $\boldsymbol{\Gamma}(\boldsymbol{x}(t_f), t_f) = \mathbf{0}$ *for the terminal boundary condition. The end-point function in this case becomes*

$$G \triangleq \boldsymbol{\Phi}(\boldsymbol{x}(t_f), t_f) + \boldsymbol{\nu}^T \boldsymbol{\Gamma}(\boldsymbol{x}(t_f), t_f) \tag{10}$$

with the vector of constant Lagrange multipliers $\boldsymbol{\nu} \in \mathbb{R}^q$.

A. First-Order Necessary Conditions for Hypersonic Glide Vehicle

The point mass equations-of-motion for an un-powered vehicle flying above a non-rotating, spherical Earth are found in Reference [15] and are included here for completeness

$$\dot{V}_T = -\frac{D}{m} - g\sin\gamma \tag{11}$$

$$\dot{\gamma} = \frac{L\cos\mu}{mV_T} - \left(\frac{g}{V_T} - \frac{V_T}{R}\right)\cos\gamma \tag{12}$$

$$\dot{\chi} = \frac{L\sin\mu}{mV_T\cos\gamma} + \frac{V_T}{R}\cos\gamma\tan\phi\sin\chi \tag{13}$$

$$\dot{h} = V_T\sin\gamma \tag{14}$$

$$\dot{\phi} = \frac{V_T\cos\gamma\cos\chi}{R} \tag{15}$$

$$\dot{\Lambda} = \frac{V_T\cos\gamma\sin\chi}{R\cos\phi} \tag{16}$$

where V_T is the airspeed, γ is the flight path angle relative to the local horizontal, χ is the heading of the velocity vector measured positive clockwise from North, h is the altitude above the Earth's surface, ϕ is the latitude, and Λ is the longitude. The lift and drag are respectively given by $L = (1/2)\rho(h)V_T^2SC_L(\alpha, M)$, $D = (1/2)\rho(h)V_T^2SC_D(\alpha, M)$, where M is the Mach number. The controls are defined to be the angle-of-attack, α, and the aerodynamic bank angle, μ. The acceleration due to gravity is defined as

$$g = g_0\left(\frac{R_E}{R_E + h}\right)^2 \tag{17}$$

where R_E is the Earth's radius. Furthermore, because $R \triangleq R_E + h$, then $\dot{h} = \dot{R}$ in the equations of motion.

From Equation 3 the controls must satisfy:

$$\frac{\partial \mathscr{H}}{\partial \alpha} = 0 = -\frac{\lambda_V}{m}\frac{\partial D}{\partial \alpha} + \frac{\partial L}{\partial \alpha}\left(\frac{\lambda_\gamma\cos\mu}{mV_T} + \frac{\lambda_\chi\sin\mu}{mV_T\cos\gamma}\right) \tag{18}$$

$$\frac{\partial \mathscr{H}}{\partial \mu} = 0 = \frac{L}{mV_T}\left(-\lambda_\gamma\sin\mu + \frac{\lambda_\chi\cos\mu}{\cos\gamma}\right) \tag{19}$$

Equation 19 can be re-written as follows since the lift will not in general be zero,

$$-\lambda_\gamma\sin\mu + \frac{\lambda_\chi\cos\mu}{\cos\gamma} = 0 \tag{20}$$

Equation 20 can also be solved in terms of the bank angle

$$\tan\mu = \frac{\lambda_\chi}{\lambda_\gamma\cos\gamma} \tag{21}$$

Equation 20 is then used to eliminate either λ_χ or λ_γ from Equation 18. Choosing to eliminate λ_χ gives the following function for angle-of-attack

$$-\lambda_V\frac{\partial D}{\partial \alpha} + \frac{\partial L}{\partial \alpha}\frac{\lambda_\gamma}{V_T\cos\mu} = 0 \tag{22}$$

Alternatively, since both lift and drag are functions of angle-of-attack, Equation 22 can be re-written as

$$\frac{\partial D}{\partial L} = \frac{\partial C_D}{\partial C_L} = \frac{\lambda_\gamma \sec\mu}{V_T \lambda_V} \tag{23}$$

Expanding the Euler-Lagrange Equations for the co-states, applying Equations 20 and 22 where appropriate, and simplifying gives the following:

$$\begin{aligned}\dot{\lambda}_V = -\Bigg\{ &+\lambda_\gamma \left[-\frac{L\cos\mu}{mV_T^2} - \left(-\frac{g}{V_T^2} - \frac{1}{R} \right) \cos\gamma \right] + \lambda_\chi \left[-\frac{L\sin\mu}{mV_T^2\cos\gamma} + \frac{\cos\gamma\sin\chi\tan\phi}{R} \right] \\ &+ \lambda_h \sin\gamma + \lambda_\phi \frac{\cos\gamma\cos\chi}{R} + \lambda_\Lambda \frac{\cos\gamma\sin\chi}{R\cos\phi} \Bigg\}\end{aligned} \tag{24}$$

$$\begin{aligned}\dot{\lambda}_\gamma = -\Bigg\{ &\left(-\lambda_V g + \lambda_h V_T \right) \cos\gamma + \lambda_\gamma \left(\frac{g}{V_T} - \frac{V_T}{R} \right) \sin\gamma - \lambda_\Lambda \frac{V_T \sin\gamma\sin\chi}{R\cos\phi} \\ &+ \lambda_\chi \left(\frac{L\sin\mu}{mV_T} \frac{\sin\gamma}{\cos^2\gamma} - \frac{V_T}{R} \sin\gamma\sin\chi\tan\phi \right) - \lambda_\phi \frac{V_T}{R} \sin\gamma\cos\chi \Bigg\}\end{aligned} \tag{25}$$

$$\dot{\lambda}_\chi = -\frac{V_T\cos\gamma}{R} \left[\left(\lambda_\chi \sin\phi + \lambda_\Lambda \right) \sec\phi\cos\chi - \lambda_\phi \sin\chi \right] \tag{26}$$

$$\dot{\lambda}_\phi = -\frac{V_T\cos\gamma\sin\chi}{R\cos^2\phi} \left(\lambda_\chi + \lambda_\Lambda \sin\phi \right) \tag{27}$$

$$\dot{\lambda}_\Lambda = 0 \tag{28}$$

$$\dot{\lambda}_h = \frac{2g}{R} \left(\lambda_V \sin\gamma - \lambda_\gamma \cos\gamma \right) + \frac{V_T\cos\gamma}{R} \left[-\lambda_\gamma + \left(\lambda_\chi \sin\phi + \lambda_\Lambda \right) \frac{\sin\chi}{\cos\phi} + \lambda_\phi \cos\chi \right] \tag{29}$$

The terminal boundary conditions for the co-states are computed from Equations 7 and 8. Assuming that the longitude and the altitude will be specified at the final time, with all other states free, and that the cost is $J = -\phi(t_f)$, the terminal boundary conditions are:

$$h(t_f) = 0 \tag{30}$$

$$\Lambda(t_f) = \Lambda_f \tag{31}$$

$$\lambda_V(t_f) = 0 \tag{32}$$

$$\lambda_\gamma(t_f) = 0 \tag{33}$$

$$\lambda_\chi(t_f) = 0 \tag{34}$$

$$\lambda_h(t_f) = \nu_h \tag{35}$$

$$\lambda_\Lambda = \nu_\Lambda \tag{36}$$

$$\lambda_\phi(t_f) = -1 \tag{37}$$

$$\mathscr{H}(t_f) = 0 \tag{38}$$

The Lagrange multipliers ν_h and ν_Λ are unknowns. The terminal value of the Hamiltonian comes from Equation 4.

III. Noether's Theorem and Its Application

A first integral of a system of differential equations is defined as a function that is constant along all extremal curves. Applying Noether's Theorem to a system of differential equation allows one to determine any first integrals of that system that may exist. This is done through the application of a transformation in either the independent variable t and/or the dependent variables $\boldsymbol{x}$.

Given a functional

$$J(\boldsymbol{x}) = \int_{t_0}^{t_f} F(t, \boldsymbol{x}, \dot{\boldsymbol{x}}) dt \tag{39}$$

and a transformation

$$t^* = \Phi(t, \boldsymbol{x}, \dot{\boldsymbol{x}}) \tag{40}$$
$$\boldsymbol{x}^* = \boldsymbol{\Psi}(t, \boldsymbol{x}, \dot{\boldsymbol{x}}) \tag{41}$$

then the functional is said to be invariant under the transformation if

$$\int_{t_0^*}^{t_f^*} F(t^*, \boldsymbol{x}^*, \dot{\boldsymbol{x}}^*)\, dt^* = \int_{t_0}^{t_f} F(t, \boldsymbol{x}, \dot{\boldsymbol{x}})\, dt \tag{42}$$

Theorem 1 (Noether's Theorem[16]) *If the functional*

$$J(\boldsymbol{x}) = \int_{t_0}^{t_f} F(t, \boldsymbol{x}, \dot{\boldsymbol{x}})\, dt \tag{43}$$

is invariant under the transformations above for arbitrary t_0 and t_f, then

$$\frac{\partial F}{\partial \dot{\boldsymbol{x}}}^T \boldsymbol{\psi} + \left(F - \dot{\boldsymbol{x}}^T \frac{\partial F}{\partial \dot{\boldsymbol{x}}} \right) \varphi = const \tag{44}$$

where

$$\varphi = \left. \frac{\partial \Phi(t, \boldsymbol{x}, \dot{\boldsymbol{x}}; \epsilon)}{\partial \epsilon} \right|_{\epsilon=0} \tag{45}$$

$$\boldsymbol{\psi} = \left. \frac{\partial \Psi(t, \boldsymbol{x}, \dot{\boldsymbol{x}}; \epsilon)}{\partial \epsilon} \right|_{\epsilon=0} \tag{46}$$

In other words, every one parameter family of transformations leaving $J(\boldsymbol{x})$ invariant leads to a first integral of its Euler equations.

Proof 1 *The proof can be found in Reference [16].*

To apply Noether's Thereom, it can be shown that Equation 44 can also be restated in terms of the Hamiltonian and the co-states $\boldsymbol{\lambda}$ by using a Legendre Transformation

$$\boldsymbol{\lambda}^T \boldsymbol{\psi} - \mathscr{H} \varphi = \text{const} \tag{47}$$

If ϵ is a small quantity, then in the most general case,

$$t^* = t + \epsilon \varphi(t, \boldsymbol{x}, \dot{\boldsymbol{x}}) + o(\epsilon) \tag{48}$$
$$\boldsymbol{x}^* = \boldsymbol{x} + \epsilon \boldsymbol{\psi}(t, \boldsymbol{x}, \dot{\boldsymbol{x}}) + o(\epsilon) \tag{49}$$

From the above equations $\delta t = \epsilon \varphi$ and $\delta \boldsymbol{x} = \epsilon \boldsymbol{\psi}$, and Equation 47 then becomes

$$\boldsymbol{\lambda}^T \delta \boldsymbol{x} - \mathscr{H} \delta t = \text{const} \tag{50}$$

Using Equation 50, two different cases are examined. First, if $F(t, \boldsymbol{x}, \dot{\boldsymbol{x}})$, or equivalently the corresponding Hamiltonian, is *not* an explicit function of t and one takes the transformation

$$t^* = t + \epsilon$$
$$\boldsymbol{x}^* = \boldsymbol{x}$$

resulting in $\varphi = 1$, and $\boldsymbol{\psi} = \mathbf{0}$, then the Hamiltonian can be shown to be a constant along each extremal.

In the second case, relaxing the assumption that t appears explicitly in the function $F(t, \boldsymbol{x}, \dot{\boldsymbol{x}})$ and applying the transformation

$$t^* = t$$
$$\boldsymbol{x}^* = \boldsymbol{x} + \boldsymbol{\epsilon}$$

gives $\varphi = 0$ and $\psi_i = 1$ if $\epsilon_i \neq 0$, and 0 otherwise. Equation 50 then simplifies to the form utilized by Moyer[10, 11]

$$\boldsymbol{\lambda}^T \delta \boldsymbol{x} = \text{const} \tag{51}$$

Remark 2 *Note that Noether's Theorem only holds for weak variations (Reference [10]). From Bryson and Ho,[14] a weak variation is defined as a variation where* $\|\boldsymbol{\delta x}\|^2 = 0$ *and* $\|\boldsymbol{\delta \dot{x}}\|^2 = 0$.

Remark 3 *Although this paper is addressing optimal control problems of the Mayer type, Noether's Theorem still applies. This is because any end-point cost can be rewritten in terms of a running cost.*

Remark 4 *A necessary and sufficient condition for an arbitrary function* Ψ *to be a first integral of the Euler equations is that the Poisson Bracket of* Ψ *and the Hamiltonian,* $\mathscr{H}$

$$[\Psi, \mathscr{H}] = \sum_{i=1}^{n} \frac{\partial \Psi}{\partial x_i} \frac{\partial \mathscr{H}}{\partial \lambda_i} - \frac{\partial \Psi}{\partial \lambda_i} \frac{\partial \mathscr{H}}{\partial x_i}$$

vanishes identically.

A. Application of Noether's Theorem

In this section, Moyer's approach (Reference [11]) of employing infinitesimal rotations one at a time to compute the integrals-of-motion using Noether's Theorem is described. The derivation is formally included here in order to resolve sign differences in the integrals-of-motion determined by Moyer and those derived in this paper. The differences in the constants arise due to how the respective coordinate systems are defined.

For this analysis, we define an Earth-centered, Earth-fixed (ECEF) coordinate system where $\hat{\boldsymbol{\imath}}$ lies in the plane of the equator and passes through the Prime Meridian. The unit vector $\hat{\boldsymbol{k}}$ points toward the North Pole, and finally, $\hat{\boldsymbol{\imath}} \times \hat{\boldsymbol{\jmath}} = \hat{\boldsymbol{k}}$ defines the ECEF frame. The position of the vehicle will be defined using a spherical coordinate system. The longitude Λ is defined as a positive (Eastward) rotation about $\hat{\boldsymbol{k}}$ and the latitude ϕ is a positive rotation above the equatorial plane. The corresponding position is then

$$\boldsymbol{r} = R\cos\Lambda\cos\phi\hat{\boldsymbol{\imath}} + R\sin\Lambda\cos\phi\hat{\boldsymbol{\jmath}} + R\sin\phi\hat{\boldsymbol{k}}$$

where $R \triangleq R_E + h$, R_E is the Earth's mean radius, and h is the altitude of the vehicle above the Earth's surface.

To apply Noether's theorem, define the variation of the position vector in spherical coordinates

$$\begin{aligned}\delta\boldsymbol{r} =& \delta R(\cos\Lambda\cos\phi\hat{\boldsymbol{\imath}} + \sin\Lambda\cos\phi\hat{\boldsymbol{\jmath}} + \sin\phi\hat{\boldsymbol{k}}) + \\ & R\delta\phi(-\sin\phi\cos\Lambda\hat{\boldsymbol{\imath}} - \sin\phi\sin\Lambda\hat{\boldsymbol{\jmath}} + \cos\phi\hat{\boldsymbol{k}}) + \\ & R\delta\Lambda(-\cos\phi\sin\Lambda\hat{\boldsymbol{\imath}} + \cos\phi\cos\Lambda\hat{\boldsymbol{\jmath}})\end{aligned} \tag{52}$$

Note that the position vector $\boldsymbol{r}$ also describes the origin of a plane attached to the center-of-mass of the vehicle. This is a local-vertical, local-horizontal plane that is normal to the radial vector described above.

This frame is oriented such that $\hat{\boldsymbol{n}}_1$ points due North, $\hat{\boldsymbol{n}}_2$ is due East, and $\hat{\boldsymbol{n}}_3$ is positive towards the center of the Earth. The aircraft's velocity vector projected onto this unit triad is then

$$\boldsymbol{V}_T = V_T(\cos\gamma\cos\chi\hat{\boldsymbol{n}}_1 + \cos\gamma\sin\chi\hat{\boldsymbol{n}}_2 - \sin\gamma\hat{\boldsymbol{n}}_3)$$

where γ is the inclination of the velocity vector above the LVLH plane, and χ is the orientation or heading of the velocity vector on the plane. Note that in this case, a zero heading means the aircraft is flying due North. The rotation matrix from the LVLH frame to the ECEF frame is

$$\boldsymbol{R}_{E/L} = \begin{bmatrix} -\sin\phi\cos\Lambda & -\sin\Lambda & -\cos\phi\cos\Lambda \\ -\sin\phi\sin\Lambda & \cos\Lambda & -\cos\phi\sin\Lambda \\ \cos\phi & 0 & -\sin\phi \end{bmatrix}$$

The variation of the velocity of the vehicle in the ECEF frame is then found in the same manner and is straight-forward.

1. Infinitesimal Rotation about Polar Axis

The first rotation that will be examined is a rotation about the polar or $\hat{\boldsymbol{k}}$ axis of magnitude ϵ. The variation due to the infinitesimal rotation can be written as the product of a skew-symmetric (cross-product) matrix and the position vector (Reference [17])

$$\delta\boldsymbol{r} = \delta\boldsymbol{\Omega}\boldsymbol{r}$$

where

$$\delta\boldsymbol{\Omega} = \begin{bmatrix} 0 & \delta\Omega_z & -\delta\Omega_y \\ -\delta\Omega_z & 0 & \delta\Omega_x \\ \delta\Omega_y & -\delta\Omega_x & 0 \end{bmatrix}$$

Letting $\delta\Omega_x = \delta\Omega_y = 0$ and $\delta\Omega_z = \epsilon$ gives the result

$$\begin{aligned} \delta x &= \epsilon R\cos\phi\sin\Lambda \\ \delta y &= -\epsilon R\cos\phi\cos\Lambda \\ \delta z &= 0 \end{aligned}$$

From Equation 52, equate like components of the vector $\delta\boldsymbol{r}$ to those immediately above.

$$\begin{aligned} \epsilon R\cos\phi\sin\Lambda &= \delta R\cos\Lambda\cos\phi - R\delta\phi\sin\phi\cos\Lambda - R\delta\Lambda\cos\phi\sin\Lambda \\ \epsilon R\cos\phi\cos\Lambda &= \delta R\sin\Lambda\cos\phi - R\delta\phi\sin\phi\sin\Lambda + R\delta\Lambda\cos\phi\cos\Lambda \\ 0 &= \delta R\sin\phi + R\delta\phi\cos\phi \end{aligned}$$

Solving the above three equations for δR, $\delta\phi$, and $\delta\Lambda$ gives $\delta R = \delta\phi = 0$, and $\delta\Lambda = -\epsilon$. This process is then repeated for the velocity in the ECEF frame replacing the position vector and its variation where appropriate. The result is that $\delta V = \delta\gamma = \delta\chi = 0$.

Now, substituting into $\boldsymbol{\lambda}^T\boldsymbol{\delta x} = c_3'$ where c_3' is a constant (the convention used in this paper is that the subscript on the constant indicates the axis about which the infinitesimal rotation occurs) yields the following integral

$$\lambda_\Lambda = -c_3'/\epsilon = c_3$$

This integral is also evident from the derivation of the first-order necessary conditions for optimality since

$$\dot{\lambda}_\Lambda = -\frac{\partial\mathscr{H}}{\partial\Lambda} = 0$$

One then simply repeats the process for rotations about the x and y axes, which yields the following two integrals-of-motion for the system:

$$c_1' = \epsilon\left[\lambda_\phi \cos\Lambda + \sin\Lambda \sec\phi\left(\lambda_\chi + \lambda_\Lambda \sin\phi\right)\right] \tag{53}$$

$$c_2' = \epsilon\left[-\lambda_\phi \sin\Lambda + \cos\Lambda \sec\phi\left(\lambda_\chi + \lambda_\Lambda \sin\phi\right)\right] \tag{54}$$

From Equations 53 and 54, it is evident that these equations can be solved to yield closed-form solutions for λ_χ and λ_ϕ

$$\lambda_\phi = c_2 \cos\Lambda - c_1 \sin\Lambda \tag{55}$$

$$\lambda_\chi = -\lambda_\Lambda \sin\phi + \cos\phi\left(c_1 \cos\Lambda + c_2 \sin\Lambda\right) \tag{56}$$

The constants c_1 and c_2 are simply c_1'/ϵ and c_2'/ϵ and are determined by the terminal boundary conditions for λ_ϕ and λ_χ.

If we assume the most general case where the terminal values of the latitude, longitude, and heading are specified, and using the following endpoint function for the optimal control problem

$$G = \mathbf{\Phi}(\boldsymbol{x}(t_f), t_f) + \nu_\chi(\chi(t_f) - \chi_f) + \nu_\phi(\phi(t_f) - \phi_f) + \nu_\Lambda(\Lambda(t_f) - \Lambda_f)$$

it can be shown that

$$\frac{\partial G}{\partial \chi_f} = \frac{\partial \mathbf{\Phi}}{\partial \chi} + \nu_\chi = \lambda_\chi(t_f)$$
$$\frac{\partial G}{\partial \phi_f} = \frac{\partial \mathbf{\Phi}}{\partial \phi} + \nu_\phi = \lambda_\phi(t_f)$$
$$\frac{\partial G}{\partial \Lambda_f} = \frac{\partial \mathbf{\Phi}}{\partial \Lambda} + \nu_\Lambda = \lambda_\Lambda(t_f)$$

Therefore, for a given $\Lambda_f = \Lambda(t_f)$ and $\phi_f = \phi(t_f)$, the general expressions for the latitude and heading co-states are

$$\lambda_\phi(t) = \lambda_\phi(t_f)\cos(\Lambda - \Lambda_f) - \sec\phi_f \sin(\Lambda - \Lambda_f)[\lambda_\chi(t_f) + \lambda_\Lambda \sin\phi_f] \tag{57}$$

$$\lambda_\chi(t) = \lambda_\phi(t_f)\cos\phi \sin(\Lambda - \Lambda_f) - \lambda_\Lambda \sin\phi + \cos(\Lambda - \Lambda_f)\cos\phi \sec\phi_f[\lambda_\chi(t_f) + \lambda_\Lambda \sin\phi_f)] \tag{58}$$

Additionally, because time does not explicitly appear in the Hamiltonian, it is an additional integral-of-motion. The value of the Hamiltonian depends upon Equation 4.

IV. Solution of Minimum Energy Optimal Footprint

In this section, we will describe a new homotopy approach for an indirect numerical method to solve for the minimum energy footprint. Although a study of the execution times was not conducted, the expected benefit to be realized is a reduction of the execution time that results from *improved* initial guesses for the co-states. The approach uses a neural network to predict the initial conditions of the co-states by leveraging the integrals-of-motion c_1 and c_2 along the footprint. The co-state associated with longitude, λ_Λ, is used as a sweeping parameter, since this co-state is directly related to the final longitude. This differs from the traditional approach of solving each individual trajectory using the final longitude as a sweeping parameter,

but provides the same result while decreasing the dimension of the search space for the co-state initial conditions.

The footprint problem is one of a class of minimum energy optimal control problems of interest for re-entry vehicles and for hypersonic test vehicles. In the case of re-entry vehicles, the footprint is computed to a desired energy state to determine alternate landing sites if there is a hardware failure such as a stuck control effector that increases the rate of energy dissipation due to a reduced lift-to-drag ratio, or some other anomaly. The energy condition (velocity and altitude) needs to be satisfied in order to begin the transition from the re-entry phase to the terminal area energy management and approach and landing phases. Lu and Xue[1] have cast this particular footprint determination problem as one of minimizing the distance to a target latitude-longitude pair that is outside the actual footprint while achieving the specified terminal energy.

On the other hand, for a hypersonic test vehicle, the size of the footprint dictates whether range safety requirements will require a flight termination system. The footprint in this case is the maximum crossrange for a given downrange that can be achieved by *minimizing* the energy when the altitude is zero. For the reachability footprint, the terminal velocity is allowed to be free. The cost function is the same for both cases, which is to maximize cross range (lateral deviation) for a prescribed downrange, and is defined along a great circle ground track. (Note that for an arbitrary initial heading, a coordinate transformation can be used to define an equivalent problem of flying along the equator). Also, terminal heading and flight path angle are allowed to be free. From the end-point conditions, it can be shown that $\lambda_\phi(t_f) = -1$ and $\lambda_\chi(t_f) = 0$. Using Equations 58 and 57, this gives us the following analytical expressions for these two co-states:

$$\lambda_\phi(t) = \lambda_\Lambda \sin(\Lambda - \Lambda_f) \tan\phi_f - \cos(\Lambda - \Lambda_f) \tag{59}$$

$$\lambda_\chi(t) = \lambda_\Lambda[\sin\phi - \cos\phi \tan\phi_f \cos(\Lambda - \Lambda_f)] - \cos\phi \sin(\Lambda - \Lambda_f) \tag{60}$$

which can be used in place of the differential equations for these two co-states.

In principle we have a total of four integrals-of-motion, including the Hamiltonian, and therefore should be able to eliminate four of the co-state differential equations as there are four closed form solutions, leaving two differential equations for the co-states that need to be solved. While this is obvious, it does not reduce the number of unknowns (initial conditions on the co-states) that must be found to solve the problem using an indirect method. Therefore, an alternate approach is taken that allows one to take advantage of the expressions for c_1 and c_2 and how their values change for each trajectory that defines a given footprint in order to improve the *guesses* for the co-state initial conditions.

A. Numerical Method

An examination of several footprints for a hypersonic vehicle were studied that included a fixed set of initial conditions with varying initial heading, and two different initial energy conditions. The behavior of the co-states at $t = 0$ and the integrals-of-motion were then analyzed for the various optimal trajectories that were computed. It is known that when $\lambda_\Lambda = 0$, the resulting optimal trajectory corresponds to one that either maximizes or minimizes the latitude for the entire footprint. What is also important is that this result is independent of the initial heading, and would in fact correspond to the maximum downrange if the initial heading were due North.

Figure 1 shows a partial footprint and the corresponding altitude time histories for each trajectory for a hypersonic vehicle initially flying due West. The dashed line in each plot corresponds to the maximum crossrange trajectory, so the longitude co-state $\lambda_\Lambda = 0$. In the altitude plot, notice that the vehicle initially wants to dive then climb in a phugoid-type of motion.

The corresponding optimal angle-of-attack and bank angle time histories are shown in Figure 2. Again, the dashed line in each plot corresponds to the maximum crossrange trajectory. The controls are typical of what is seen for these trajectories, especially the behavior at the terminal point of the trajectory. Those trajectories that fly for a longer time than the maximum crossrange trajectory correspond to $\lambda_\Lambda > 0$ and

increase as λ_Λ increases. The shorter trajectories correspond to $\lambda_\Lambda < 0$ and decrease as the longitude co-state becomes more negative. In the case of angle-of-attack, both the velocity and flight-path angle co-states tend to zero, albeit at different rates. Physically, the aircraft wants to increase lift to extend the range, so it increases angle-of-attack. The bank angle eventually becomes monotonic as it goes to zero due to the fact the final heading is free, so the heading co-state $\lambda_\chi(t_f) = 0$.

In Figure 3, the terminal longitude and latitude are given as functions of the sweeping parameter λ_Λ. The longitude can be fit reasonably well with an arc-tangent function, although it is not shown here. On the other hand a seventh-order polynomial is a good approximation for this curve. In Figures 4 and 5, the integrals of optimal motion are also shown to be well behaved across footprints with varying initial headings, implying that the calculation of c_1 and c_2 will likely not be a significant challenge. In Figure 6, the co-states are given as functions of the sweeping parameter λ_Λ for various initial headings. Since the co-states are relatively well behaved, it is expected that improved initial guesses to an indirect solver can be constructed using a nonlinear prediction method based on these data.

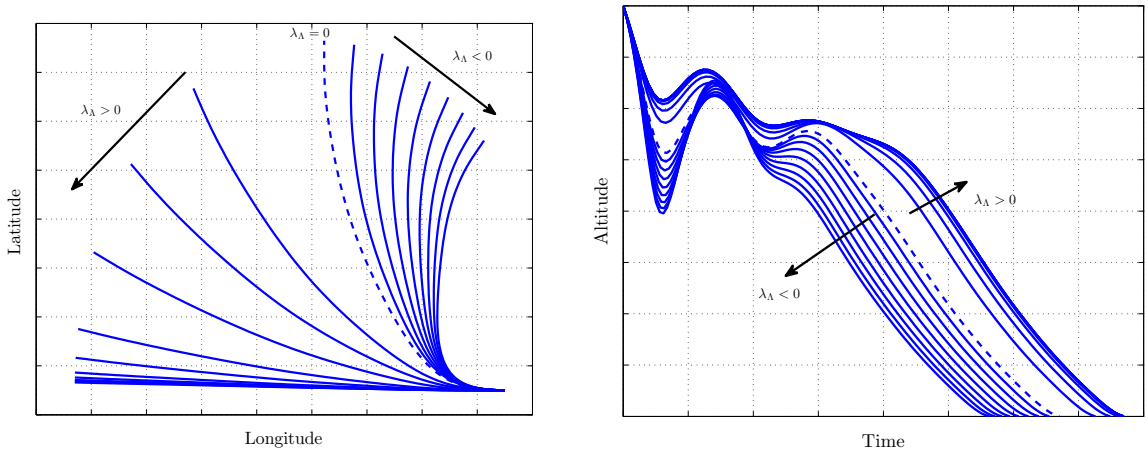

(a) Latitude vs. Longitude (b) Altitude

Figure 1. Reachability Footprint Trajectories, Initial Heading Due West ($\chi_0 = -90$ deg)

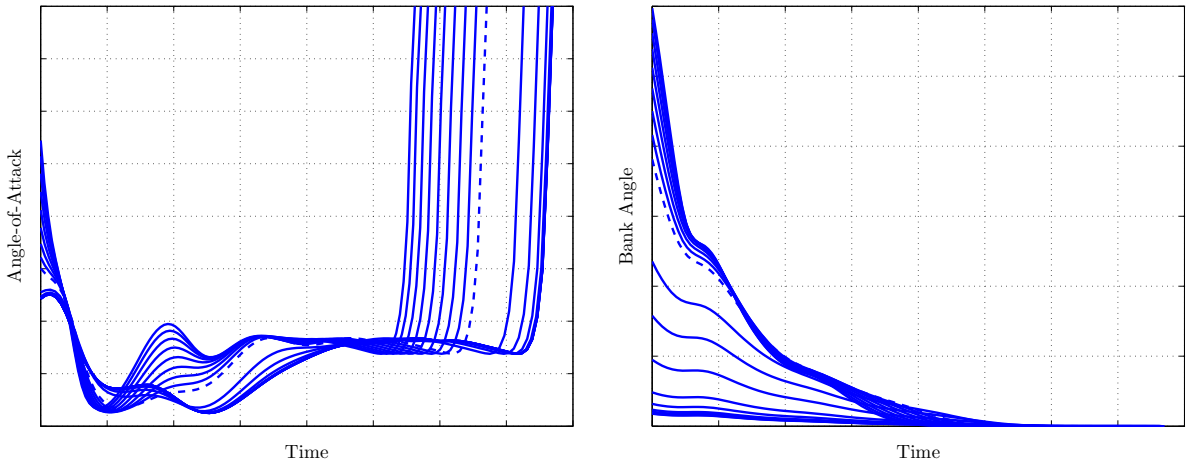

(a) Angle-of-Attack (b) Bank Angle

Figure 2. Reachability Footprint Controls, Initial Heading Due West

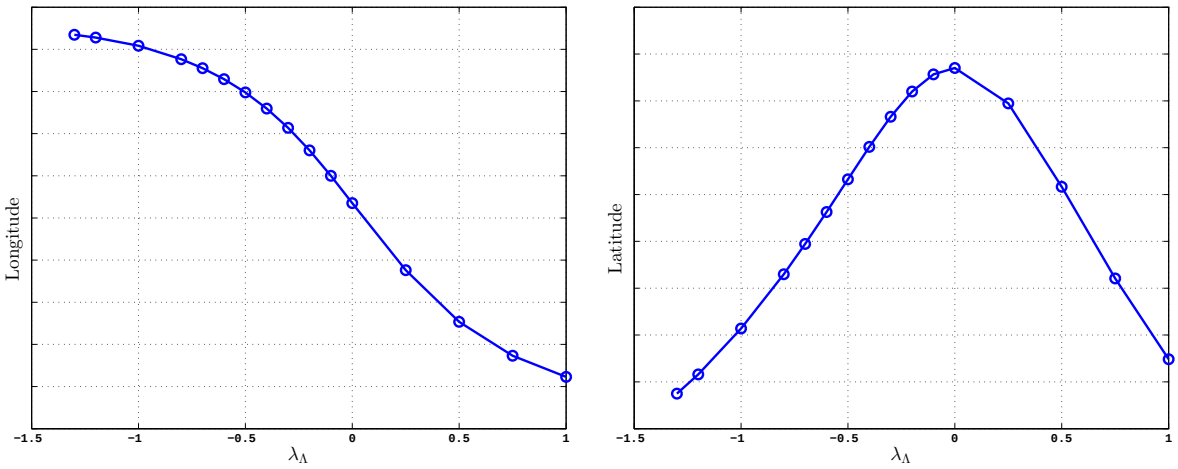

(a) Longitude (b) Latitude

Figure 3. Variation of Longitude and Latitude with λ_Λ (Half-Footprint), Initial Heading Due West

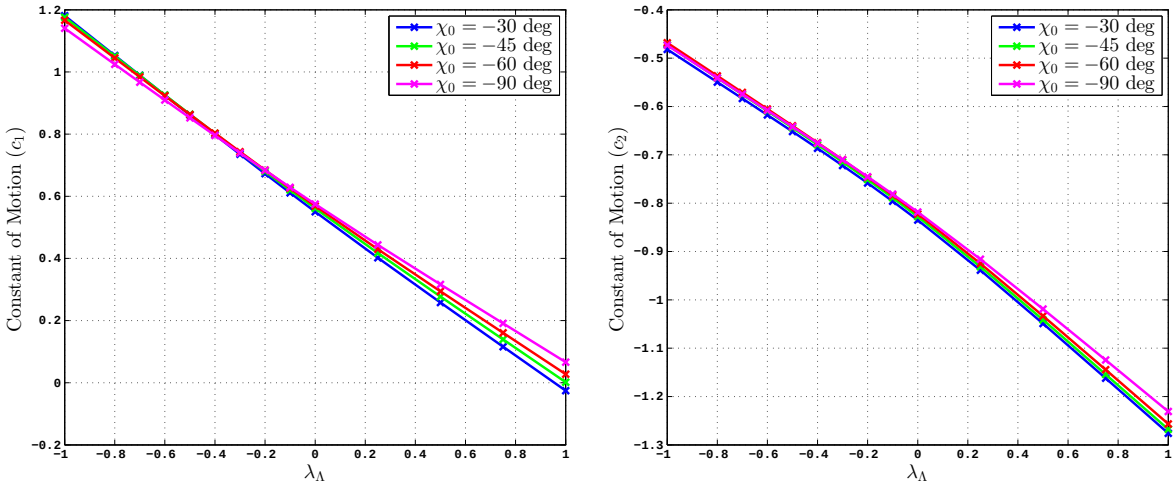

(a) c_1 (b) c_2

Figure 4. Integrals-of-Motion as a Function of λ_Λ and Initial Heading

B. High Quality Predictions Using An Artificial Neural Network

To provide accurate initial guesses for the unknown initial co-states, a nonlinear prediction model can be created. Since the initial co-states are well-behaved, it is expected that many nonlinear prediction methods would be suitable. For this investigation, a neural network was created to provide accurate initial co-state estimates along the hypersonic trajectory. Traditionally, a neural network is used to provide predictions of complex systems in the absence of underlying physical theory. While the physics of the optimal hypersonic footprint problem are known (as described in Section A), numerically solving the boundary value problem is extremely challenging. As such, the neural network must be constructed in a manner that provides high confidence of the optimality associated with the predicted initial co-states.

For direct trajectory optimization applications, the quality of a neural network's fit is determined numerically by testing an independent set of validation cases.[18,19] While these cases are often expansive across the input space, the approach does not provide confidence that the neural network will also provide accurate predictions for non-validated inputs. As such, it is necessary to validate the model for the infinitely many

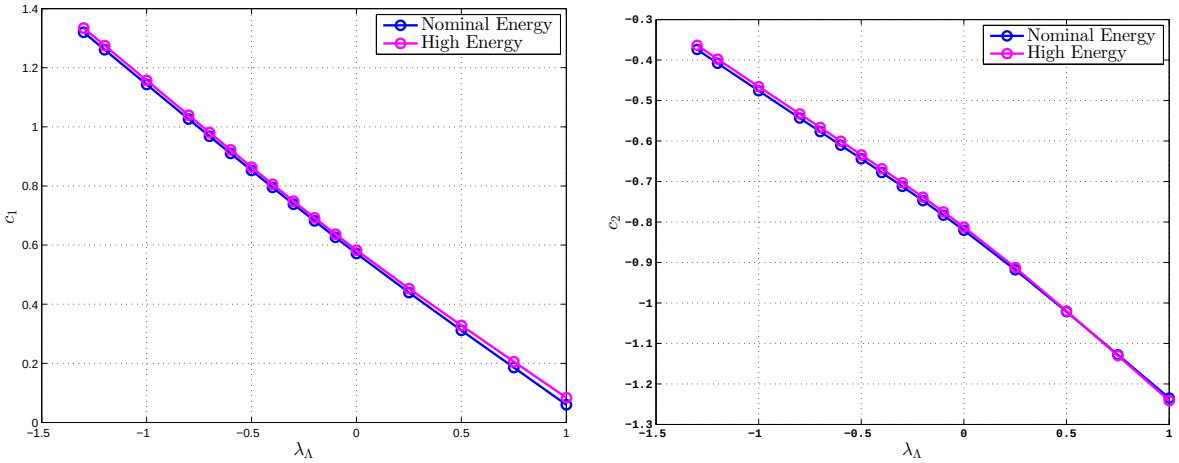

(a) c_1 (b) c_2

Figure 5. Integrals-of-Motion as a Function of λ_Λ and Initial Energy, Initial Heading Due West

possible input combinations that may be passed to the neural network. The formulation of the optimization problem as a boundary value problem (provided by the indirect approach) enables a unique opportunity to analytically evaluate the quality of the predictions across the infinitely many input combinations using the process described below.

1. Neural Network Training

To train the neural network, a training set of data is created by numerically solving the optimal control problem as shown in Section A where the initial states are selected to surround an expected hypersonic trajectory. Using these data, a neural network that consists of a single hidden layer with 12 nodes (described by Figure 7) is trained to predict the unknown co-states at the initial location of the trajectory. The hidden nodes are chosen to have the standard logistic sigmoid activation function and the output nodes are chosen to have the standard linear activation function. Since the footprint analysis is conducted over a non-rotating, spherical Earth, only the footprint associated with an initial latitude and longitude of zero degrees and due West heading is considered. It is expected that this footprint could be appropriately rotated across the spherical surface to the appropriate location due to varying initial latitudes, longitudes, and headings. As such, a neural network could be created across a wide range of anticipated initial states in altitude, velocity, and flight-path angle as well as the footprint sweeping parameter, λ_Λ, to predict the remaining unknown initial co-states and the propagation time, t_f, as described by Equations 61-66.

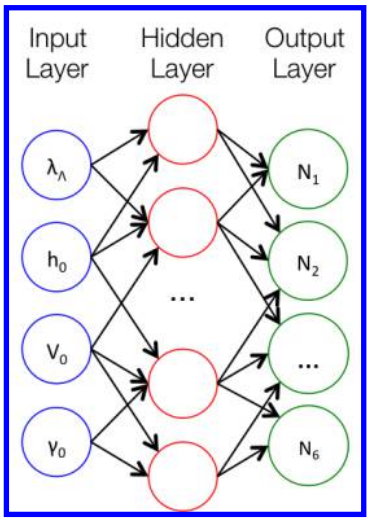

Figure 7. Notional Diagram of a Neural Network

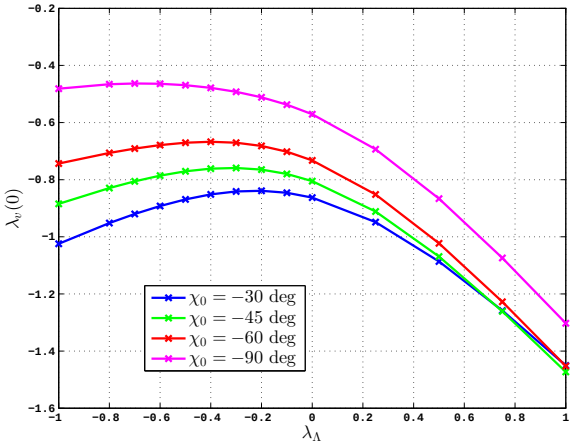

(a) $\lambda_v(0)$

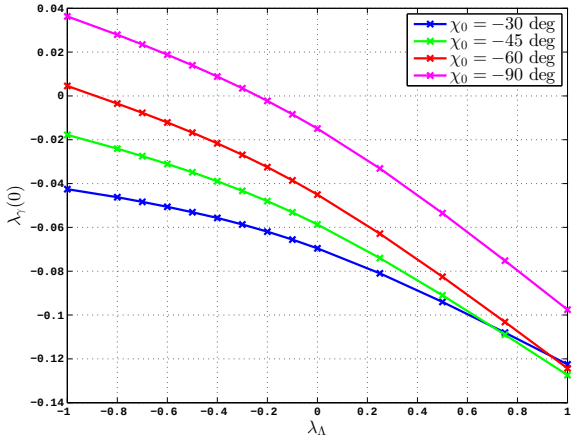

(b) $\lambda_\gamma(0)$

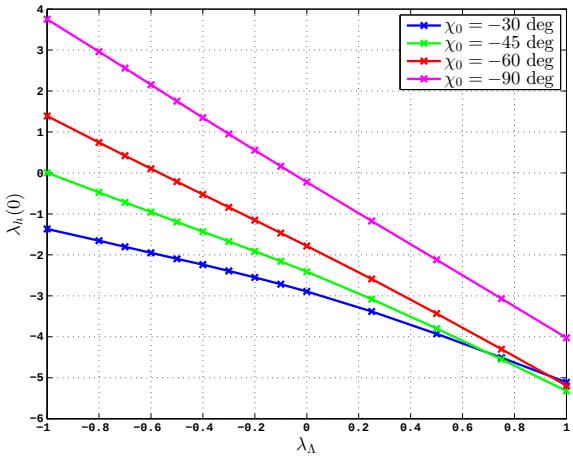

(c) $\lambda_h(0)$

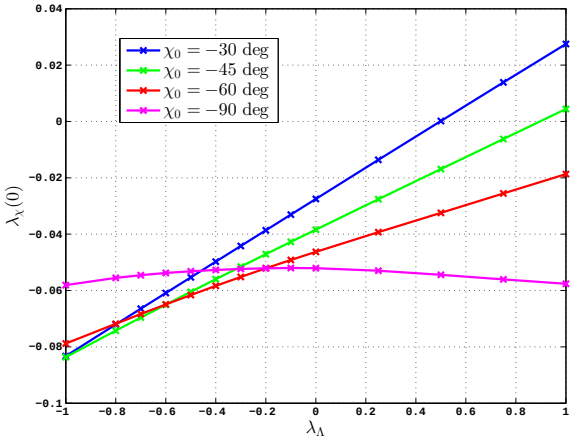

(d) $\lambda_\chi(0)$

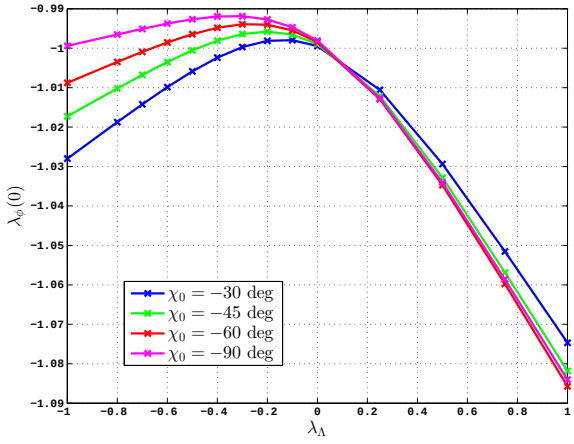

(e) $\lambda_\phi(0)$

Figure 6. Initial Co-states as a Function of Longitude Co-state and Initial Heading

$$\lambda_{V_T}(t_0) \approx \mathscr{N}_1(\lambda_\Lambda, h_0, V_{T,0}, \gamma_0) \tag{61}$$
$$\lambda_\gamma(t_0) \approx \mathscr{N}_2(\lambda_\Lambda, h_0, V_{T,0}, \gamma_0) \tag{62}$$
$$\lambda_\chi(t_0) \approx \mathscr{N}_3(\lambda_\Lambda, h_0, V_{T,0}, \gamma_0) \tag{63}$$
$$\lambda_h(t_0) \approx \mathscr{N}_4(\lambda_\Lambda, h_0, V_{T,0}, \gamma_0) \tag{64}$$
$$\lambda_\phi(t_0) \approx \mathscr{N}_5(\lambda_\Lambda, h_0, V_{T,0}, \gamma_0) \tag{65}$$
$$t_f \approx \mathscr{N}_6(\lambda_\Lambda, h_0, V_{T,0}, \gamma_0) \tag{66}$$

It is important to note that the integrals-of-motion, c_1 and c_2, can be predicted separately by quadratic curve fits due to the relatively consistent behaviors with respect to λ_Λ for the due West trajectory and range of flight energies as shown in Figures 4 and 5. As such, a curve fit is created for each integral-of-motion as shown in Equations 67 and 68, and these integrals can be used to compute $\lambda_\phi(t_0)$ and $\lambda_\chi(t_0)$ directly from Equations 55 and 56 rather than from the neural network as described by Equations 63 and 65. The integrals-of-motion play a key role in reducing the dimensionality of the neural network predictions, resulting in the reduced system shown in Equations 69-72. This reduction greatly simplifies the training and validation of the network.

$$c_1 = c_{1,0} + c_{1,\lambda_\Lambda}\lambda_\Lambda + c_{1,\lambda_\Lambda^2}\lambda_\Lambda^2 \tag{67}$$
$$c_2 = c_{2,0} + c_{2,\lambda_\Lambda}\lambda_\Lambda + c_{2,\lambda_\Lambda^2}\lambda_\Lambda^2 \tag{68}$$
$$\lambda_{V_T}(t_0) \approx \mathscr{N}_1(\lambda_\Lambda, h_0, V_{T,0}, \gamma_0) \tag{69}$$
$$\lambda_\gamma(t_0) \approx \mathscr{N}_2(\lambda_\Lambda, h_0, V_{T,0}, \gamma_0) \tag{70}$$
$$\lambda_h(t_0) \approx \mathscr{N}_3(\lambda_\Lambda, h_0, V_{T,0}, \gamma_0) \tag{71}$$
$$t_f \approx \mathscr{N}_4(\lambda_\Lambda, h_0, V_{T,0}, \gamma_0) \tag{72}$$

Since the co-states are well behaved, the neural network was verified to provide a good fit to the training data. This is illustrated in Figure 8 for the initial co-state predictions for a high energy hypersonic vehicle initially traveling due West. On average, each neural network evaluation required 5 ms on a modern, dual-core laptop. The rapid prediction of initial co-states could be used within time sensitive applications that require the rapid generation of optimal footprints. To ensure that the neural network provides high quality predictions across all possible input combinations, a verification process is employed that makes use of the analytic theory from the necessary conditions of optimality.

2. Artificial Neural Network Validation

During the training process, the data from optimal indirect trajectories are passed through the neural network, and the corresponding numerical predictions are compared to the indirect data. This process creates a set of numerical weights and biases within the neural network that accurately predicts the numerical data. To verify the quality of the neural network across the infinitely many possible input combinations, a symbolic representation of each input is passed through the neural network. Since the neural network consists of a combination of arithmetic and exponential operations, the output of the neural network (described by Equations 69-72) can also be represented as complex symbolic expressions. This distinction is notionally described in Figure 9 for inputs x and y and outputs a and b. Additionally, symbolic predictions of c_1 and c_2 can be created from the quadratic curve fits (Equations 67 and 68).

Since the optimal footprint problem is not an explicit function of time, the Hamiltonian retains a constant value across all optimal footprint trajectories. As such, the terminal boundary condition $\mathscr{H}(t_f) = 0$ implies that the Hamiltonian is also zero at the initial point of the trajectory. This is a particularly useful result.

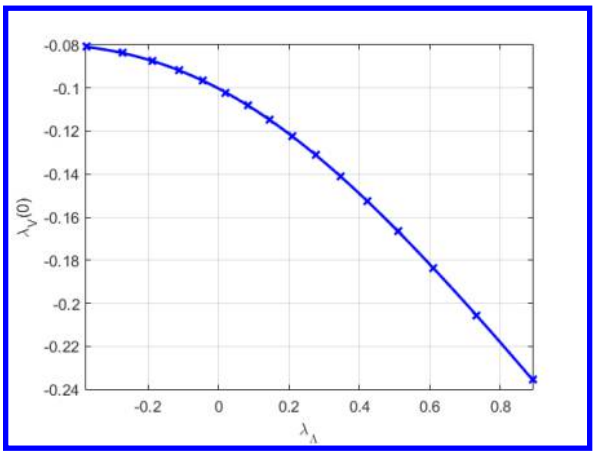

(a) $\lambda_v(0)$ vs. λ_Λ

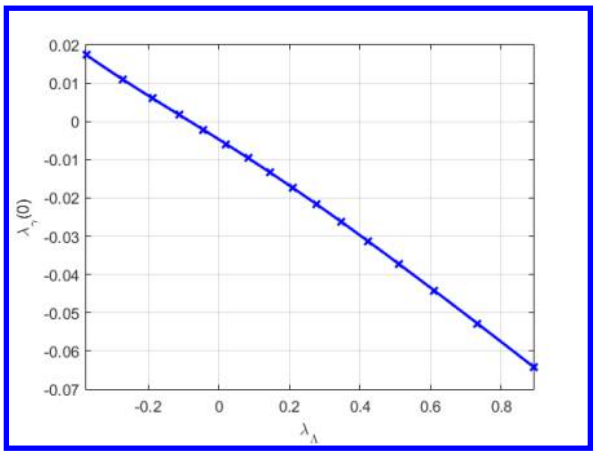

(b) $\lambda_\gamma(0)$ vs. λ_Λ

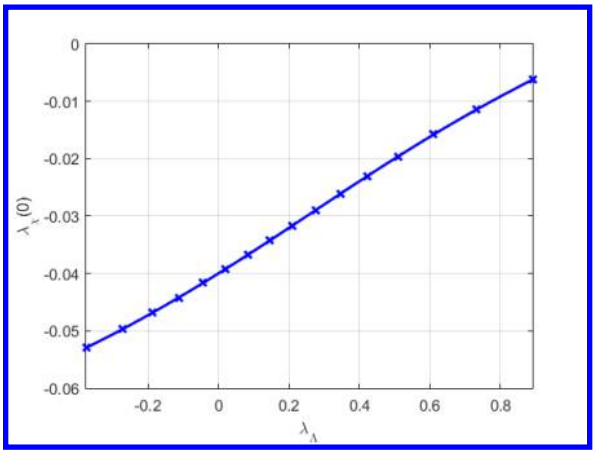

(c) $\lambda_\chi(0)$ vs. λ_Λ

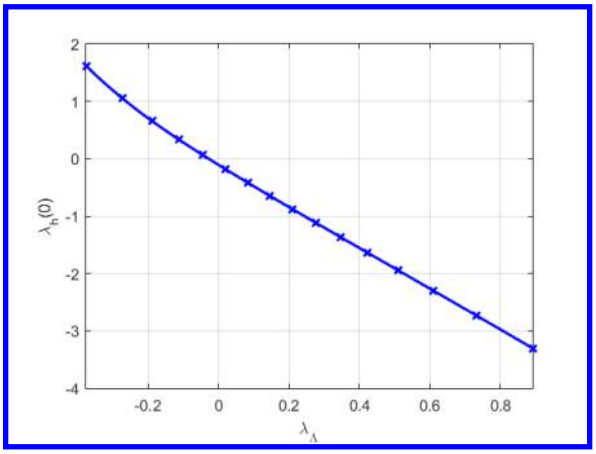

(d) $\lambda_h(0)$ vs. λ_Λ

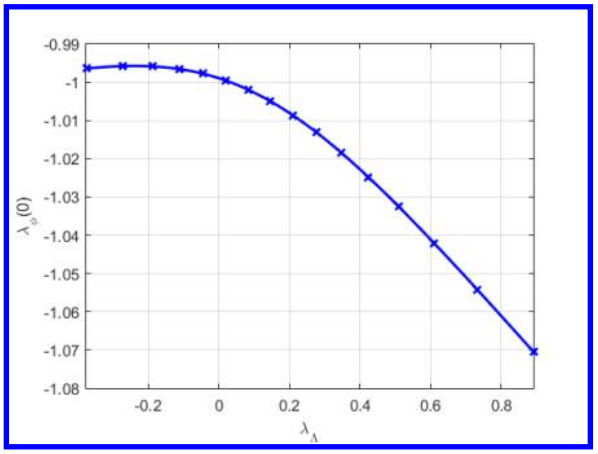

(e) $\lambda_\phi(0)$ vs. λ_Λ

Figure 8. Predicted Initial Co-States as a Function of the Sweeping Parameter, λ_Λ.

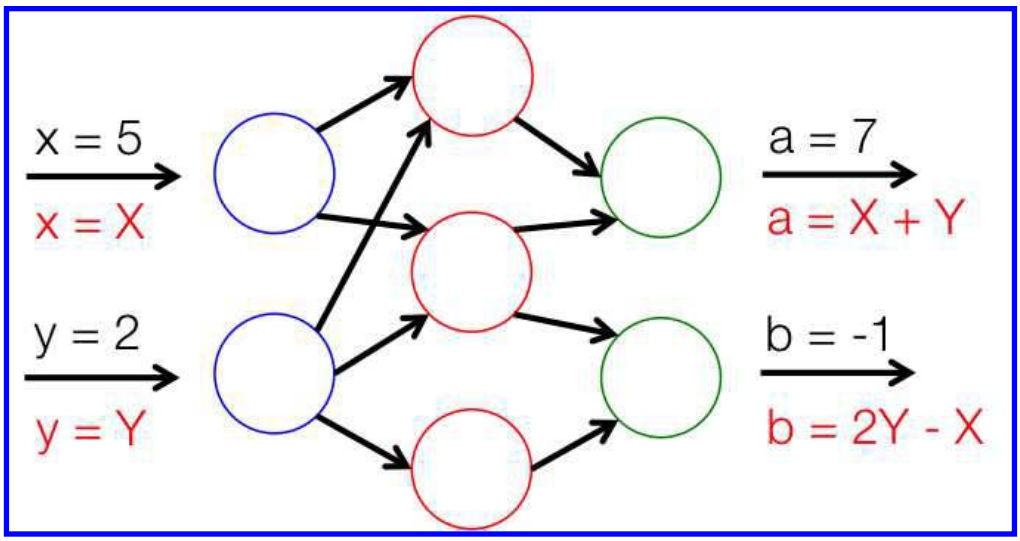

Figure 9. Notional Difference Between Numerical and Symbolic Evaluation of the Neural Network

In general, the initial Hamiltonian can be analytically expressed as a function of the initial states and co-states. Since the predicted initial co-states can be represented symbolically as a function of the inputs to the neural network and quadratic curve fits, then the initial Hamiltonian condition can be expressed as shown in Equation 73.

$$\mathscr{H}(V_T(t_0), \gamma(t_0), h(t_0), \lambda_\Lambda(t_0)) = 0 \tag{73}$$

If the maximum residual in the initial Hamiltonian can be determined analytically, then an assessment can be made regarding the quality of the neural network. More importantly, an analytic assessment of the maximum residual of the initial Hamiltonian would effectively assess the infinitely many combinations of possible inputs to the neural network. This unique analytic analysis is made possible through the formulation of necessary conditions provided by indirect methods.

3. Analytic Assessment of the Initial Hamiltonian Maximum Residual

Due to the highly nonlinear expressions that are symbolically output from the neural network, it is generally not possible to develop analytic, closed-form solutions that correspond to the extrema of the residual. A purely numerical search for the maximum residual would only assess a finite number of possible input combinations, thereby negating the benefits of assessing all possible input combinations using the analytic Hamiltonian formulation. As a simple example, for a fixed initial altitude, velocity, and flight-path angle, the residual of the Hamiltonian is only a function of the remaining input to the neural network, λ_Λ. The residual in the predicted initial Hamiltonian is shown as a function of the footprint sweeping parameter in Figure 10. As expected, the Hamiltonian residual is near zero across the range of the sweeping parameter. This implies that the neural network predictions are of high quality without over-fitting to the training data. For footprints generated from a single parameter, the maximum residual in the Hamiltonian can be examined graphically. For footprints generated by the full range of inputs to the neural network, a robust analytic method is required.

To obtain approximate extrema across the entire domain of possible inputs, the analytic residual of the initial Hamiltonian is approximated using a Taylor series expansion. For example, Equation 74 illustrates the Taylor series in the sweeping parameter, λ_Λ, for a single set of initial states. The interior extrema of the residual can be determined by differentiating Equation 74 and solving for the corresponding roots. To

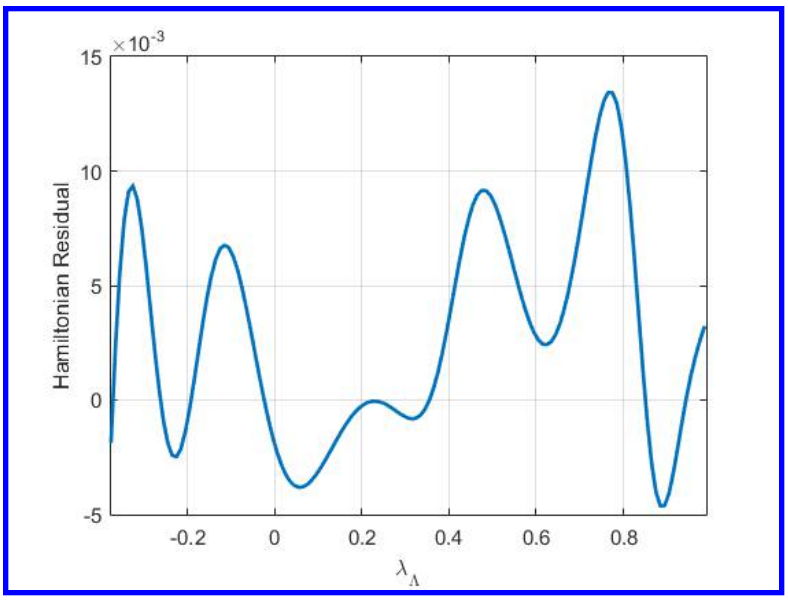

Figure 10. Residual of Predicted Hamiltonian by the Neural Network

ensure that analytic roots can be found, the original Taylor series cannot have an order greater than five. This requirement ensures that the differential is a polynomial of order four or less, thereby guaranteeing an analytic solution to the roots. The residual at the boundaries of the sweeping parameter can also be assessed to analytically determine the global extrema associated with the Taylor series approximation. This feature is particularly useful since this process effectively analyzes the infinitely many residuals associated with each possible λ_Λ.

$$\mathscr{H}(\lambda_\Lambda + \Delta\lambda_\Lambda) = \sum_{n=0}^{\infty} \frac{1}{n!} \frac{\partial^n \mathscr{H}(\lambda_\Lambda)}{\partial \lambda_\Lambda^n} (\Delta\lambda_\Lambda)^n \tag{74}$$

Due to the highly nonlinear Hamiltonian residual (see Figure 10), a single, fifth order Taylor series approximation across the entire input domain will be inaccurate. To be confident of the maximum residual computed as described above, the accuracy of the Taylor series expressions must be verified. To create accurate Taylor series approximations, the range of possible inputs is divided into intervals, and a unique Taylor series approximation is created within each interval. As an example, the Hamiltonian residual is segmented according to the sweeping parameter, λ_Λ, as shown in Figure 11 for various numbers of intervals, where the blue x's correspond to the centers of each interval. For large segments that correspond to a small number of intervals, many of the example fifth order Taylor series approximations are not accurate. However, as the segments are chosen to be sufficiently small (corresponding to a sufficiently large number of intervals), then the Taylor series approximations are very accurate. As such, a process must be created to verify that the regions are chosen sufficiently small such that the Taylor series approximations converge to the actual residual with sufficient accuracy.

To assess the accuracy of the Taylor series approximations, the process described above is performed across a wide range of numbers of intervals. For each choice in the number of intervals, the maximum residual across all intervals is recorded as shown in Figure 12. If the maximum residual is observed to converge as the number of intervals is increased, then the Taylor series within each interval is assumed to have also converged. After this process is completed, the maximum residual corresponding to the highest number of intervals is recorded. This recorded maximum residual essentially provides a worst case residual of the initial Hamiltonian. If this maximum residual is sufficiently small, then the neural network is expected to provide sufficiently accurate predictions of the optimal initial co-states across the infinitely many possible

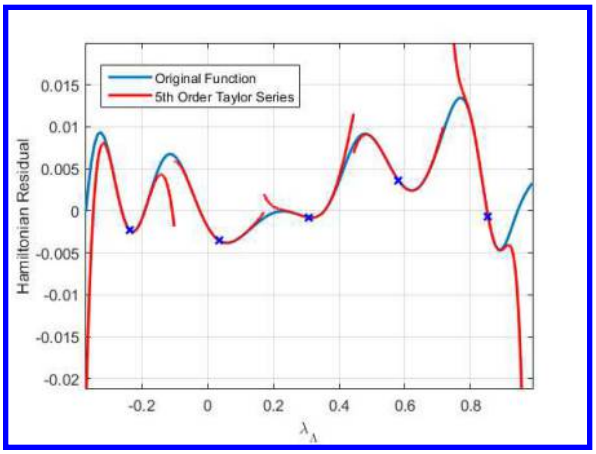

(a) 6 intervals

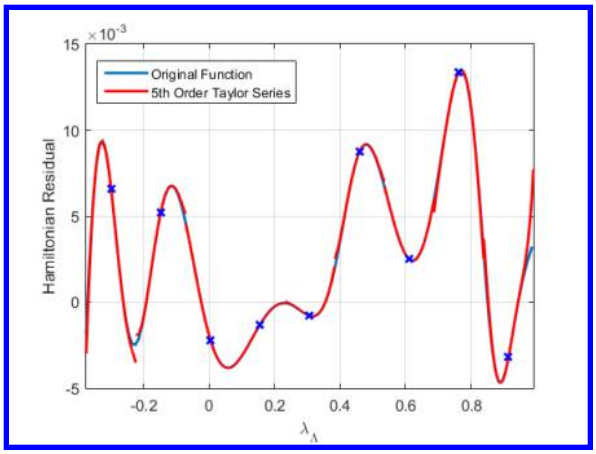

(b) 10 intervals

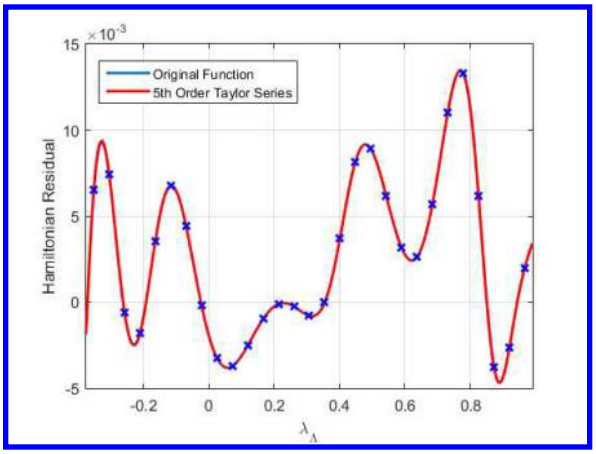

(c) 30 intervals

Figure 11. Taylor Series Approximations of the Hamiltonian Residual for Different Numbers of Intervals

inputs.

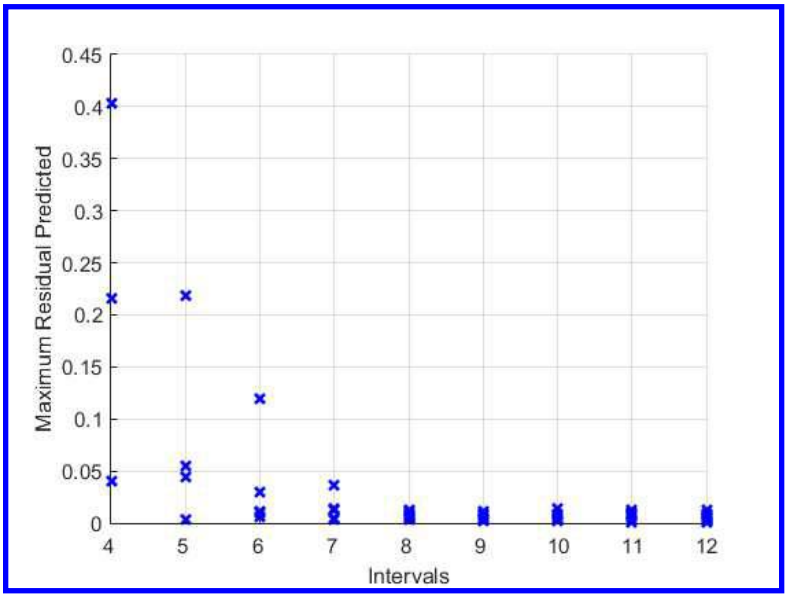

Figure 12. Maximum Residual of Predicted Hamiltonian by the Taylor Series Segments

This process for a single input can be extended to an arbitrary number of dimensions. For the general four-dimensional input of the neural network shown in Equations 69-72, the Taylor series approximations can be constructed as described in Equation 75. Multidimensional intervals are then constructed throughout the range of inputs to the neural network defined by the set of hypersonic trajectories of interest. The residual of Taylor series approximations are then interrogated across a range of interval sizes. To simplify the higher dimensional root-solving process after differentiating Equation 75, only second order Taylor series approximations were leveraged. The maximum residual of the initial Hamiltonian as function of the number of intervals along one of the four dimensions is shown in Figure 13. Equally spaced intervals were constructed that span the four dimensions, resulting in a maximum of $7^4 = 2,401$ intervals in this analysis. The maximum predicted residual converges as the number of intervals used to generate the Taylor series approximations increases, indicating that a high quality neural network is created to predict the optimal initial co-states to support footprint generation across a wide range of expected trajectories.

$$\mathscr{H} = \sum_{n_1=0}^{\infty}\sum_{n_2=0}^{\infty}\sum_{n_3=0}^{\infty}\sum_{n_4=0}^{\infty}\frac{1}{n_1!n_2!n_3!n_4!}\frac{\partial^{(n_1+n_2+n_3+n_4)}\mathscr{H}(V_{T,0},\gamma_0,h_0,\lambda_\Lambda)}{\partial V_{T,0}^{n_1}\partial\gamma_0^{n_2}\partial h_0^{n_3}\partial\lambda_\Lambda^{n_4}}\Delta V_{T,0}^{n_1}\Delta\gamma_0^{n_2}\Delta h_0^{n_3}\Delta\lambda_\Lambda^{n_4} \tag{75}$$

With verified high quality initial co-state predictions, the neural network could be used in parallel to generate a large set of initial co-states that correspond to the many footprint trajectories associated with a particular state of the hypersonic vehicle. As such, each trajectory that resides on the maximum footprint can be propagated in parallel, thereby avoiding the sequential creation of trajectories associated with a homotopy in λ_Λ. This parallel feature would enable the rapid creation of various footprints to support time-critical operations.

V. Conclusions

In this investigation, a methodology is created to improve the solution time of generating hypersonic footprints. A homotopy method is employed to generate optimal hypersonic footprint data using indirect optimization methods. The application of Noether's Theorem to the optimal hypersonic footprint problem

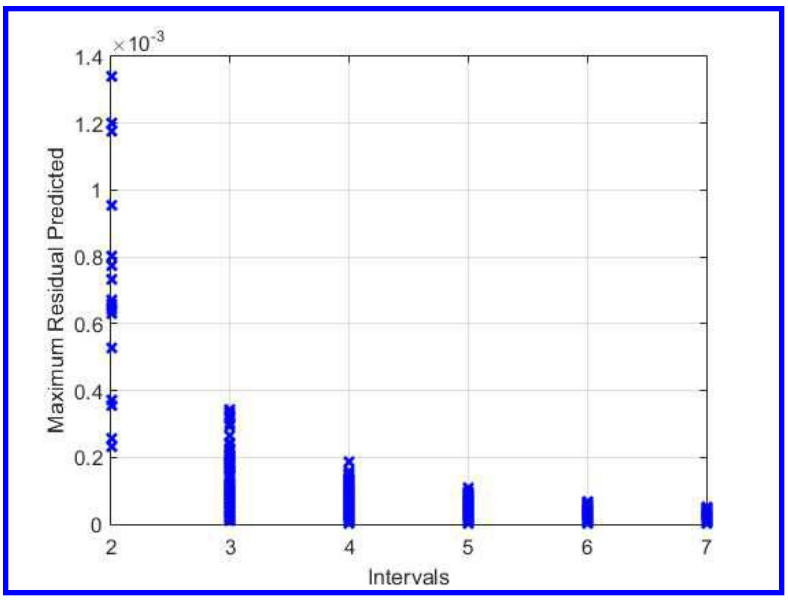

Figure 13. Maximum Residual of Predicted Hamiltonian by the Four-Dimensional Taylor Series Segments

enables the calculation of integrals-of-motion along each trajectory. Analysis of the data indicates that the integrals of motion can be easily predicted as a function of the longitude co-state. In fact, the integrals-of-motion exhibit a nearly consistent linear behavior for a wide range of trajectories. Using curve fits of the integrals-of-motion, the number of unknown initial co-states that must be predicted to generate optimal hypersonic footprint trajectories is reduced. To support time-critical operations, a neural network is created to provide highly accurate predictions of the reduced number of initial co-states associated with optimal footprint trajectories. The quality of the initial co-state predictions is verified by leveraging analytic information provided by the necessary conditions of optimality. Specifically, the maximum residual of the initial Hamiltonian can be assessed analytically across the infinitely many possible input combinations to the neural network. The small residuals associated with this analysis indicate that the initial co-state predictions by the neural network will always be of high quality. The rapid evaluation of the neural network would enable the nearly instantaneous creation of initial co-states associated with the wide range of trajectories that encompass the footprint. These trajectories can then be propagated in parallel to rapidly generate hypersonic footprints to support time-critical operations.

VI. Acknowledgements

Approved for Public Release. Distribution Unlimited. Case Number 88-ABW-2014-xxxx.

References

[1]Lu, P. and Xue, S., "Rapid Generation of Accurate Entry Landing Footprints," *Journal of Guidance, Control, and Dynamics*, Vol. 33, No. 3, May-June 2011, pp. 756–767.

[2]Harpold, J. and Graves, C., "Shuttle Entry Guidance," *The Journal of Astronautical Sciences*, Vol. 27, No. 3, 1979, pp. 239–268.

[3]Brown, K. and Johnson, G., "Real-time Optimal Guidance," *IEEE Transactions on Automatic Control*, Vol. AC-12, No. 5, October 1967, pp. 501–506.

[4]Karpenko, M., Bhatt, S., Bedrossian, N., Fleming, A., and Ross, I., "First Flight Results on Time-Optimal Spacecraft Slews," *Journal of Guidance, Control, and Dynamics*, Vol. 35, No. 2, March-April 2012, pp. 367–376.

[5]Breakwell, J. V., "The Optimization of Trajectories," *SIAM Journal*, Vol. 7, No. 2, June 1959, pp. 215–247.

[6]Vinh, N. X., Busemann, A., and Culp, R. D., *Hypersonic and Planetary Entry Flight Mechanics*, The University of Michigan Press, 1980.

[7]Fahroo, F., Doman, D., and Ngo, A., "Modeling Issues in Footprint Generation for Reusable Launch Vehicles," *2IEEE Aerospace Conference*, 2003, IEEEAC Paper Number 1436.

[8]Lu, P., Forbes, S., and Baldwin, M., "Gliding Guidance of High L/D Hypersonic Vehicles," *AIAA Guidance, Navigation, and Control Conference*, 2013, AIAA 2013-4648.

[9]Bollino, K., Ross, I., and Doman, D., "Optimal Non-linear Feedback Guidance for Reentry Vehicles," *AIAA Guidance, Navigation, and Control Conference*, 2006, AIAA 2006-6074.

[10]Moyer, H. G., "Integrals for Impulsive Orbit Transfer from Noether's Theorem," *AIAA Journal*, Vol. 7, No. 7, July 1969, pp. 1232–1235.

[11]Moyer, H. G., "Integrals for Optimal Flight Over a Spherical Earth," *AIAA Journal*, Vol. 11, No. 10, October 1973, pp. 1441–1443.

[12]Vinh, N. X., "Integrals of the Motion for Optimal Trajectories in Atmospheric Flight," *AIAA Journal*, Vol. 11, No. 5, May 1973, pp. 700–703.

[13]Vinh, N. X., "General Theory of Optimal Trajectory for Rocket Flight in a Resisting Medium," *Journal of Optimization Theory and Applications*, Vol. 11, No. 2, 1973, pp. 189–202.

[14]Bryson, A. and Ho, Y., *Applied Optimal Control*, Taylor and Francis, 1975.

[15]Bilimoria, K. and Schmidt, D., "Integrated Development of Equations-of-Motion for Elastic Hypersonic Vehicles," *Journal of Guidance, Control, and Dynamics*, Vol. 18, No. 1, Jan-Feb 1995, pp. 73–81.

[16]Gelfand, I. and Fomin, S., *Calculus of Variations*, chap. 4, Prentice-Hall, Inc., 1963, pp. 79–83.

[17]Goldstein, H., *Classical Mechanics*, chap. 4, 8, Addison-Wesley Publishing, 1953.

[18]Horn, J. F., Schmidt, E. M., Geiger, B. R., and DeAngelo, M. P., "Neural Network-Based Trajectory Optimization for Unmanned Aerial Vehicles," *Journal of Guidance, Control, and Dynamics*, Vol. 35, No. 2, March-April 2012, pp. 548–562.

[19]Chanda, S. R., Nagati, M., and Steck, J. E., "Aircraft Trajectory Control Using Artificial Neural Networks," *AIAA 34th Aerospace Sciences Meeting and Exhibit*, 1996, AIAA 96-0510.